CuAg(SO$_4$)$_2$: A doubly strongly correlated altermagnetic three-dimensional analog of the parent compounds of high-T_c cuprates

Harald O. Jeschke [1], Makoto Shimizu [2], and Igor I. Mazin [3]

[1]*Research Institute for Interdisciplinary Science, Okayama University, Okayama 700-8530, Japan*
[2]*Department of Physics, Graduate School of Science, Kyoto University, Kyoto 606-8502, Japan*
[3]*Department of Physics and Astronomy, and Quantum Science and Engineering Center, George Mason University, Fairfax, Virginia 22030, USA*

The discovery of high-temperature superconductivity (HTSC) in strongly correlated cuprates opened a new chapter in condensed matter physics, breaking existing stereotypes of what is a material base for a good superconductor ("Matthias rules"), at the same time emphasizing the richness and challenge of strongly correlated physics, personified by the most strongly correlated $3d$ ion, Cu^{2+}. A recently reported new compound, CuAg(SO$_4$)$_2$, combines in a fascinating way the same ion with the most strongly correlated $4d$ one, Ag^{2+}. In this Letter, we present a detailed analysis of electronic and magnetic properties of this material, and show that it is very different from the HTSC cuprates in several different ways, and opens a door into further research of superconductivity and magnetism, in particular altermagnetism, in strongly correlated materials.

Introduction. Four decades ago the world was tantalized by the discovery of high-critical-temperature superconductors. It was soon appreciated that a pivotal role in the physics of these materials was played by the Cu^{2+} ion in a $3d^9$ configuration, a strongly correlated spin-1/2 object with one rather localized hole in the Cu $3d_{x^2-y^2}$ orbital, and that the magnetic interaction between these ions, generated by oxygen-mediated superexchange processes and peaked in two-dimensional (2D) momentum space at $\mathbf{q} = (\pi, \pi)$, is instrumental in understanding its properties [1,2].

The initial microscopic theories of these materials, rather abundant, relied upon a simple single-band Hubbard Hamiltonian, with a Mott insulator as a parent compound [3]. However, it was then realized that, while close to Mott insulators, the parent compounds belonged to a different class, namely charge-transfer insulators (CTIs) [4]. Indeed, the top of the O-p band appeared above the lower Hubbard band (LHB), which led to important ramifications.

The Cu^{2+} valence state occurs in many natural minerals as well as in synthesized compounds. Nevertheless, the peculiar physics associated with the d^9 band occupancy inspired vigorous searches for other d^9 materials. So far, the majority of this activity was associated with Ni$^+$ compounds, also having a d^9 configuration, albeit less localized than in Cu^{2+} [5,6]. At the same time, solid state chemists had their eyes on a heavier analog of Cu^{2+}, namely Ag^{2+} [7]. The d hole in this state is also highly localized, and materials with Ag^{2+} are truly rare.

Thus, the recent experimental report of a new d^9 compound forming a new, fourth class (counting Cu^{2+}, Ni$^+$, and Ag^{2+} as the first three), CuAg(SO$_4$)$_2$ [8], opens an exciting opportunity of a new variation on the old theme: A combination of Cu^{2+} *and* Ag^{2+} in the same compound warrants close attention. Moreover, as we discuss later, magnetic order in this material belongs to a recently discovered class of altermagnets [9,10], adding an additional dimension of interest to this material. It is worth noting that the only altermagnet in this class discussed so far is La$_2$CuO$_4$, where altermagnetism appears only because of small rotations of the CuO$_6$ octahedra [11,12]. In contrast, in CuAg(SO$_4$)$_2$, as discussed below, altermagnetism appears already in the Cu-Ag sublattice.

One can summarize (Table I) the key differences distinguishing CuAg(SO$_4$)$_2$ from the parent compounds of cuprate superconductors, as demonstrated and discussed in detail in this Letter.

Given such unique properties of this just recently discovered compound, one should expect more experimental work in the nearest future. The goal of this Letter is to guide and inform this research about fundamental electronic and magnetic properties of this material. In the next section we will present and discuss its electronic structure, then we will turn to magnetic interactions in the system, and demonstrate and explain their highly unusual topology. We will then identify the stable ground state magnetic configuration and discuss its properties, including the character of spin fluctuations once the static order is suppressed (e.g., by doping). Whether such doping will indeed lead to superconductivity is unclear at the moment, but such an opportunity is quite exciting [13].

Crystal structure. The crystal structure is formed by chains aligned along the c axis of octahedral-coordinated Cu and Ag, with edge-sharing octahedra (as opposed to layered perovskite cuprates where octahedra are corner sharing), Fig. 1(a). These chains are bridged by SO$_4$ radicals, forming "molecular ligands," which are nearly ideal tetrahedra with S nearly central. The intra- as well as interchain hoppings proceed via these tetrahedra. CuO$_6$ and AgO$_6$ octahedra are strongly elongated (20% for Cu, 30% for Ag, cf. 28% in La$_2$CuO$_4$), so that the d holes reside in a well-defined $d_{x^2-y^2}$ state. Figure 1(b)
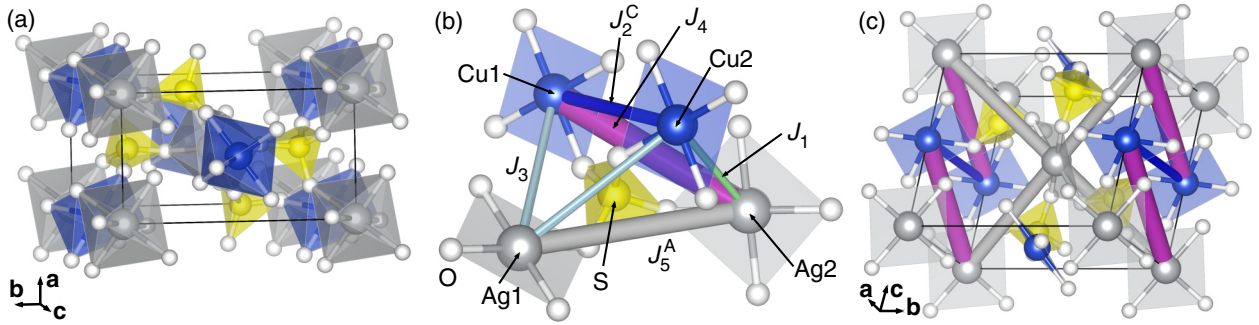
FIG. 1. (a) Crystal structure of $CuAg(SO_4)_2$ (space group $P2_1/n$, No. 14), as reported in Ref. [8]. (b) Structural unit showing only one SO_4 cluster with its nearest neighbor connected via $d_{x^2-y^2}$ orbitals. Cu and Ag sites are only numbered for use in Table II. (c) Illustration of relevant exchange paths in the structure of $CuAg(SO_4)_2$.

shows the minimal connectivity cluster, that is, an individual SO_4 tetrahedron with four metals attached to it. Interestingly, all four metal ions are positioned geometrically different, as Table II illustrates, and form different bond angles.

Electronic structure. We perform all electronic structure calculations using the full potential local orbital (FPLO) basis set [14] in combination with a generalized gradient approximation (GGA) exchange correlation functional [15]. We use a number of k points that ensures full convergence of the respective quantities which is $12 \times 12 \times 12$ for electronic structures and Fermi surfaces and $4 \times 4 \times 4$ for the large supercells used in energy mapping. The calculated band structure is shown in Fig. 2, and the corresponding density of states (DOS) in Fig. 3. For comparison, the DOS for La_2CuO_4 (calculated with the same setup) is shown in the Supplemental Material [16]. Several interesting features manifest themselves. First, due to much longer hopping paths, and strong covalent bonding in the SO_4 cluster, O bands are pushed up, compared to HTSC cuprates, and are twice narrower. As a result, 12 O p bands are separated from the rest by a full gap, and are much more pure O p than in the cuprates, while the charge-transfer (CT) gap is much larger (1.3 eV vs 0.4 eV, for the same parameter choice) and the upper Hubbard bands much narrower in $CuAg(SO_4)_2$. As a result, the metal states are more correlated, and the CT

character more pronounced than in the cuprates, promising interesting ramifications.

These new features can also be traced down to the fact that the actual "ligand" in this system is in fact the sulfate ion, which has an interesting molecular orbital structure [17,18]: one triple-degenerate t_1 orbital in each spin, which is pure O $2p$ by symmetry, and also a mixed O-S one, also a triplet, $3t_2$. The latter is the higher occupied orbital *if S 3d is not included* [17]. However, the high-lying S $3d$ pushes this state down [17], resulting in a clear separation of the upper half of the O bands, well above the metal d bands, and the lower half, overlapping the latter. What is important here is that if the system is doped by holes, they will be purely O $2p$, as opposed to cuprates, where they are considerably mixed with Cu $3d$.

One other observation from Fig. 2 is that the d bands along the Γ-R line are spin split, despite the material being antiferromagnetic (AFM), and centrosymmetric (for further evidence, see Fig. S3 in Supplemental Material [16]). Indeed, one can observe that the symmetry operation that maps the spin-up and spin-down sublattices in the $P2_1/n$ group is the n glide $(x, y, z) \rightarrow (x + \frac{1}{2}, -y + \frac{1}{2}, z + \frac{1}{2})$, while inversion maps each spin upon itself. Thus, the "glide + space inversion + time reversal" operations do not change the

TABLE I. Comparison between parent materials of cuprate superconductors and $CuAg(SO_4)_2$.

	Parent cuprates	$CuAg(SO_4)_2$
Strongly correlated species	One (Cu)	Two (Cu, Ag)
Excitation gap	Intermediate, closer to CT	Strongly CT
Leading superexchange path	Cu-O-Cu	M-SO_4-M
Leading superexchange neighbors	First	3rd, 5th, and 6th
Leading superexchange length[a]	~2.7–2.8 Å	5.7, 6.0, 4.7 Å
Dimensionality	2D	3D
Leading spin fluctuations	$\mathbf{q} = (\pi, \pi)$	$\mathbf{q} = (0, 0, 2\pi)$[b]
Altermagnetism	Sometimes[c]	Yes[d]

[a]In order of decreasing strength.
[b]In the extended Brillouin zone, corresponding to the intracell magnetic order.
[c]In La_2CuO_4 and similar materials, due to O octahedra rotations.
[d]Regardless of the presence of ligands.

TABLE II. Top: Angles formed by the M-O-S in degrees. Bottom: Angles θ in degrees, distance d in Å of the corresponding path, and calculated (see the section of magnetic interactions for details) exchange coupling constants J in K formed by M-S-M.

M	M-O-S		
Cu1	135		
Cu2	137		
Ag1	123		
Ag2	140		

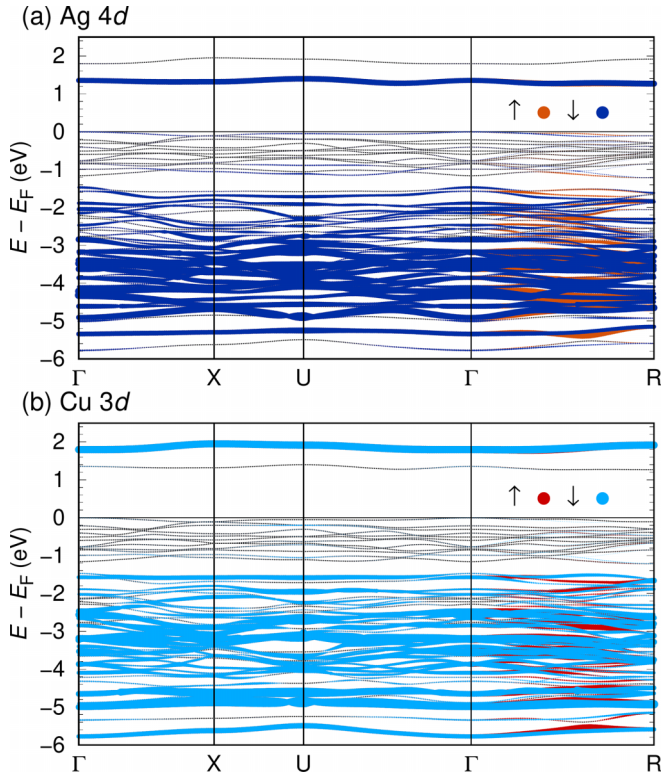|	θ (deg)	d (Å)	J (K)
Cu1-S-Cu2	96	4.73	34
Cu1-S-Ag1	102	4.96	5
Cu1-S-Ag2	122	5.73	168
Cu2-S-Ag1	102	4.96	5
Cu2-S-Ag2	66	3.58	−3
Ag1-S-Ag2	134	6.02	92

FIG. 2. GGA + U band structure of CuAg(SO$_4$)$_2$ in the lowest-energy AFM state. Colors red (spin ↑) and blue (spin ↓) indicate (a) Ag 4d orbital weights and (b) Cu 3d orbital weights. The alter-magnetic property of CuAg(SO$_4$)$_2$ is clear from the spin splitting along the Γ-R path. High symmetry points are $X = (\frac{1}{2}, 0, 0)$, $U = (\frac{1}{2}, 0, \frac{1}{2})$, $R = (\frac{1}{2}, \frac{1}{2}, \frac{1}{2})$.

magnetic structure. This operation will change the electronic state at (k_x, k_y, k_z) as $(k_x, k_y, k_z, \uparrow) \rightarrow (k_x, -k_y, k_z, \uparrow) \rightarrow (-k_x, k_y, -k_z, \uparrow) \rightarrow (k_x, -k_y, k_z, \downarrow)$ [19]. Thus, the Kramers degeneracy is preserved if $k_y = 0$ or π, consistent with the
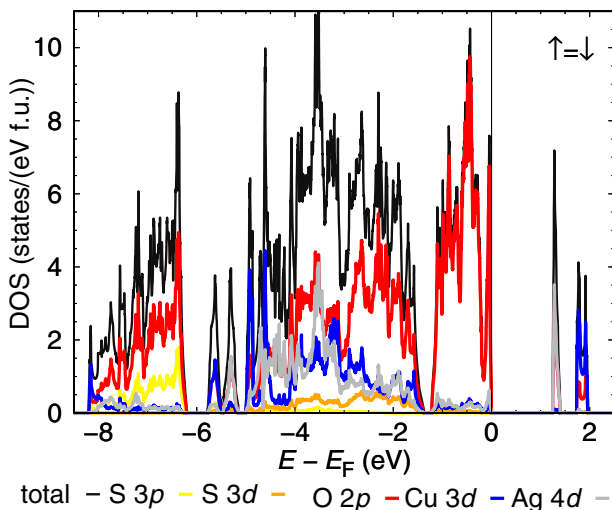

FIG. 3. GGA + U density of states per spin of CuAg(SO$_4$)$_2$ in the lowest-energy AFM state. Spin ↑ and spin ↓ are identical so only spin ↑ is shown.

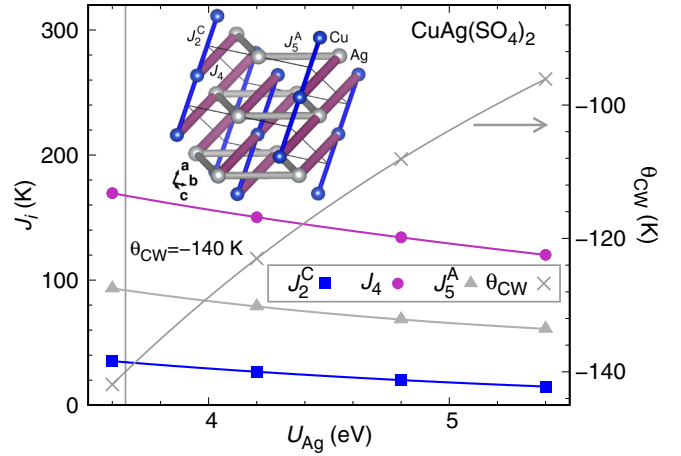FIG. 4. DFT energy mapping result for CuAg(SO$_4$)$_2$. Most important exchange interactions for four different values of on-site interaction U_{Ag} at fixed Hund's rule coupling strengths $J_H = 1$ eV for Cu and $J_H = 0.75$ eV for Ag. U_{Ag} is fixed at 75% of U_{Cu}. Inset: Exchange paths of CuAg(SO$_4$)$_2$ as defined by the three dominant exchange interactions. The width of the bonds is chosen so that cross section is proportional to the strength of the coupling.

fact that the spin splitting does not occur along the Γ-X-U-Γ line in Fig. 2 and that they are spin split along Γ-R. This is the condition for altermagnetism, a new phenomenon actively discussed recently [10,20–24]. It is worth noting that some of the cuprates, most notably La$_2$CuO$_4$, are also altermagnets, but there this feature appears as a result of the CuO$_6$ octahedra rotations [11,12], and disappears when the structure becomes tetragonal under doping. Here, however, it is robust and present even if ligands are entirely removed (the Cu-Ag sublattice still has the same symmetry).

Magnetic interactions. We determine parameters of the Heisenberg Hamiltonian $H = \sum_{i<j} J_{ij} \mathbf{S}_i \cdot \mathbf{S}_j$ for CuAg(SO$_4$)$_2$ using density functional theory (DFT) energy mapping. This approach has provided very good results for many Cu^{2+} $S = 1/2$ magnets [25–27], so we can expect it to work for CuAg(SO$_4$)$_2$ as well. It is based on a DFT + U correction [28] in order to account for strong correlations on Cu 3d and Ag 4d orbitals. We make sure to capture all relevant exchange interactions by resolving all couplings up to twice the nearest-neighbor Cu-Ag distance. For this purpose, we use a fivefold supercell containing ten formula units. For the DFT + U functional, we need on-site interactions and values of the Hund's rule coupling for both Cu^{2+} and Ag^{2+}. Between Cu 3d orbitals and Ag 4d orbitals, we introduce a factor 0.75 which is reasonable to account for the better screening in the heavier ion. For Cu^{2+}, we use the typical value $J_H^{Cu} = 1$ eV that has yielded good agreement with experiment in many cases. Figure 4(a) shows the result of the energy mapping for four values of U.

Other exchange interactions besides the three we show are 3% of the dominant coupling J_4 or less (Table III). We select values of $U_{Ag} = 3.65$ eV, $U_{Cu} = 4.87$ eV by demanding that the the full set of couplings matches the experimentally determined Curie-Weiss temperature of CuAg(SO$_4$)$_2$ which is $\theta_{CW} = -140$ K [8]. Note that these U values should be

TABLE III. Exchange parameters for CuAg(SO$_4$)$_2$ determined by DFT-based energy mapping. The on-site interaction values $U_{\text{Ag}} = 3.65$ eV and $U_{\text{Cu}} = 4.87$ eV are chosen in order to match the experimental value of the Curie-Weiss temperature of $\theta_{\text{CW}} = -140$ K [8]. The U_{Cu} is smaller than typical values for Cu^{2+} which are often in the range 6 eV $\leqslant U \leqslant$ 8 eV; this occasionally happens when U is chosen to match a θ_{CW} energy scale in energy mapping.

Name	J_1	J_2^A	J_2^C	J_3	J_4	J_5^A	J_5^C	J_6	J_7^A	J_7^C	J_8^A	J_8^C	J_{10}	J_{13}	J_{16}^A	J_{16}^C
$M1\,M2$	AgCu	AgAg	CuCu	AgCu	AgCu	AgAg	CuCu	AgCu	AgAg	CuCu	AgAg	CuCu	AgCu	AgCu	AgAg	CuCu
$d_{M1\,M2}$ (Å)	3.579	4.734		4.961	5.727	6.017		6.134	6.215		7.158		8.332	8.846	9.266	
J (K)	-3	3	34	5	168	92	-1	-3	0	-4	-2	0	0	0	1	0

viewed as internal local density approximation (LDA) $+U$ parameters and not as spectroscopic U values; they would be chosen differently if future experiments lead to a revision of the θ_{CW} value. The inset of Fig. 4 illustrates the lattice defined by J_4, $J_5^A = 0.55 J_4$ and $J_2^C = 0.20 J_4$. The Hamiltonian is dominated by antiferromagnetic Cu-Ag chains (purple) which are linked by AFM Ag-Ag square lattices. These two couplings can be satisfied by an AFM state where both Cu and Ag sublattices are AFM. However, the third strongest (but considerably smaller) coupling, an AFM Cu-Cu exchange, is moderately frustrating this Hamiltonian. We can compare our Hamiltonian parameters to the result obtained by Domanski *et al.* [8] $J_4 = 120$ K, $J_5^A = 1.08 J_4$, $J_2^C = -0.06 J_4$. A likely reason for the difference is that the approach of Ref. [8] of solving eight equations for seven exchange interactions can go astray with small inaccuracies of any one of the calculated energies.

This result seems, on the first glance, counterintuitive. The strongest coupling comes from the fifth neighbors, and the two shortest bonds contribute practically nothing. To understand this we recall that the active orbitals here are $x^2 - y^2$, and replot Fig. 1(a) using instead of the metal-centered octahedra only the squares corresponding to these orbitals [Fig. 1(b)]. One can see that these orbitals do not overlap on any oxygen, thus not generating any M-O-M superexchange, but only via SO$_4^{2-}$ ions. This yields five longer-range superexchange paths, which include the three leading ones, plus two more that appear to be numerically small due to accidental cancellation of various hopping processes. As discussed in the previous section, electronically this material is in a strong charge-transfer regime, so that instead of the standard Anderson's

superexchange proportional to $t^4/(E_d - E_p)^2 U$, where $E_d - E_p \gg U$, and t is the characteristic metal-ligand hopping, one gets [29] t^4/Δ^3, with $\Delta \ll U$ (note that the charge-transfer energy Δ is smaller because the highest occupied level in sulfate is higher than in oxygen). Therefore, despite a relatively small effective M-S hopping the resulting interaction is sizable.

Susceptibility. We analyze the Hamiltonian by defining a strong coupling susceptibility [30] as $\chi(\mathbf{q}, T) = 1/[T + J(\mathbf{q})]$, where

$$
\begin{aligned}
J(\mathbf{q}) = {} & 2J_1 \cos\frac{q_z}{2} + \left(J_2^A + J_2^C\right) \cos q_x \\
& + \left(2J_3 \cos\frac{q_x}{2} + \left(J_7^A + J_7^C\right) \cos\frac{q_x - q_z}{2}\right. \\
& \left. + \left(J_5^A + J_5^C\right) \cos\frac{q_x + q_z}{2}\right) 2\cos\frac{q_y}{2} \\
& + 2J_4 \cos\left(q_x + \frac{q_z}{2}\right) + 2J_6 \cos\left(q_x - \frac{q_z}{2}\right) \\
& + \left(J_8^A + J_8^C\right) \cos q_z.
\end{aligned}
$$

This susceptibility has maxima that are extended diagonally around $\mathbf{q} = (0, 0, 2\pi)$ in the $(q_x, 0, q_z)$ plane as shown in Fig. 5(a). There are weak maxima, marked by red dots, which are shifted from $\mathbf{q} = (0, 0, 2\pi)$ to $\mathbf{q} = (0.603, 0, 0.986)\pi$ and $\mathbf{q} = (-0.603, 0, 3.014)\pi$.

Classical Monte Carlo. We perform classical Monte Carlo calculations for the Heisenberg Hamiltonian parameters given in Table III. We perform the standard single spin-flip technique with the Metropolis updates. The result is shown
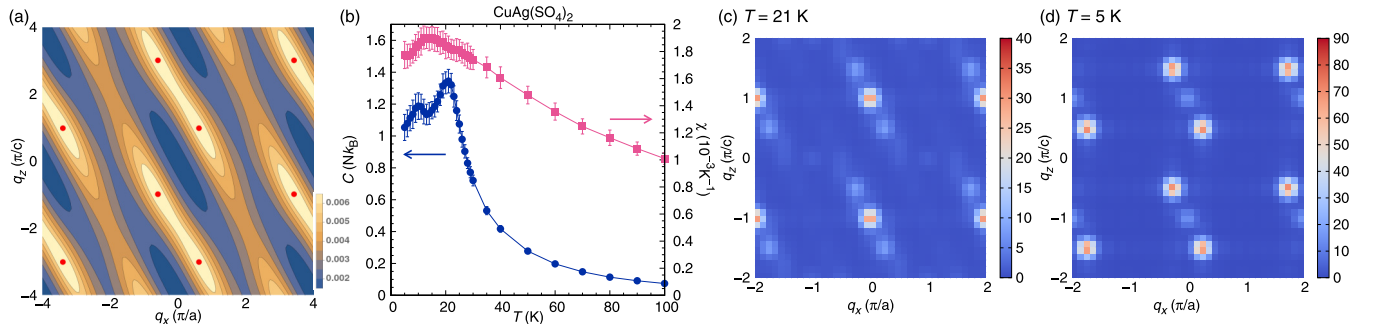

FIG. 5. Susceptibility and classical Monte Carlo (CMC) results for CuAg(SO$_4$)$_2$. (a) Susceptibility $\chi(\mathbf{q}, T)$ of CuAg(SO$_4$)$_2$ at $T = 300$ K estimated using Eq. (1). (b) CMC specific heat and susceptibility. (c) and (d) correspond to spin structure factors at $T = 21$ K and $T = 5$ K, respectively. Note that for the $\mathbf{q}$ vectors in (a), (c), and (d) we neglect the small monoclinic angle of 94° and the difference in a and c lattice parameters.

in Figs. 5(b)–5(d). The specific heat shows two peaks at $T = 21$ K and at $T = 10$ K. This indicates that even though the two dominant exchange couplings J_4 and J_5^A are unfrustrated, the frustrating coupling J_2^C leads to a significant reduction of the ordering temperature compared to the Curie-Weiss temperature of $\theta_{CW} = -140$ K. This is in good agreement with experiment where the material shows a pronounced ordering peak at $T = 40.4$ K. The peaks in the susceptibility [Fig. 5(b)] are less clearly separated. The type of ordering can be understood from Figs. 5(c) and 5(d). Upon lowering the temperature, the dominant instability is at $\mathbf{q} = (0, 0, 2\pi)$ [Fig. 5(c)]. When T is lowered further, the weak corrections due to the frustration present in the Hamiltonian kick in, increasing the weight slightly away from $\mathbf{q} = (0, 0, 2\pi)$ [Fig. 5(d)]. Thus, the second ordering peak corresponds to the weak maxima marked by red dots in Fig. 5(a).

Conclusions. We have investigated the electronic structure and magnetic properties of the recently discovered CuAg(SO$_4$)$_2$ compound, which combines strongly correlated Cu^{2+} and Ag^{2+} ions. This material bears many similarities with high-T_c cuprates, but also a number of remarkable differences, outlined in Table I. The differences stem from the fact that in this compound the sulfate ion SO$_4^{2-}$ plays the ligand role, as opposed to oxygen. As a result, the relevant hopping

and exchange paths are longer range, the antiferromagnetic ground state is highly unusual, and potential hole doping proceeds via pure O p bands (rather than a hybridized Cu-O band, as in the cuprates). In addition, the ground state is altermagnetic, that is to say, sports spin-split Cu d bands (which, however, as mentioned, are considerably removed from the Fermi level).

This collection of highly unusual properties make CuAg(SO$_4$)$_2$ a fertile playground for exotic magnetism and superconductivity (under doping); while these are beyond the scope of the current Letter, we hope that it will inspire further experimental and theoretical studies in this direction.

[1] E. Dagotto, Correlated electrons in high-temperature superconductors, Rev. Mod. Phys. **66**, 763 (1994).

[2] M. Imada, A. Fujimori, and Y. Tokura, Metal-insulator transitions, Rev. Mod. Phys. **70**, 1039 (1998).

[3] P. A. Lee, N. Nagaosa, and X.-G. Wen, Doping a Mott insulator: Physics of high-temperature superconductivity, Rev. Mod. Phys. **78**, 17 (2006).

[4] J. Zaanen, G. A. Sawatzky, and J. W. Allen, Band gaps and electronic structure of transition-metal compounds, Phys. Rev. Lett. **55**, 418 (1985).

[5] P. Hansmann, X. Yang, A. Toschi, G. Khaliullin, O. K. Andersen, and K. Held, Turning a nickelate Fermi surface into a cupratelike one through heterostructuring, Phys. Rev. Lett. **103**, 016401 (2009).

[6] D. Li, K. Lee, B. Y. Wang, M. Osada, S. Crossley, H. R. Lee, Y. Cui, Y. Hikita, and H. Y. Hwang, Superconductivity in an infinite-layer nickelate, Nature (London) **572**, 624 (2019).

[7] J. Gawraczyński, D. Kurzydlowski, R. A. Ewings, S. Bandaru, W. Gadomski, Z. Mazej, G. Ruani, I. Bergenti, T. Jaroń, A. Ozarowski, S. Hill, P. J. Leszczyński, K. Tokár, M. Derzsi, P. Barone, K. Wohlfeld, J. Lorenzana, and W. Grochala, Silver route to cuprate analogs, Proc. Natl. Acad. Sci. USA **116**, 1495 (2019).

[8] M. Domański, Z. Mazej, and W. Grochala, A unique two-dimensional silver(II) antiferromagnet Cu[Ag(SO$_4$)$_2$] and perspectives for its further modifications, Chem. Eur. J. **29**, e202302042 (2023).

[9] I. Mazin (The PRX Editors), Editorial: Altermagnetism—a new punch line of fundamental magnetism, Phys. Rev. X **12**, 040002 (2022).

[10] L. Šmejkal, J. Sinova, and T. Jungwirth, Emerging research landscape of altermagnetism, Phys. Rev. X **12**, 040501 (2022).

[11] M. Naka, Y. Motome, and H. Seo, Perovskite as a spin current generator, Phys. Rev. B **103**, 125114 (2021).

[12] L. Šmejkal, J. Sinova, and T. Jungwirth, Beyond conventional ferromagnetism and antiferromagnetism: A phase with nonrelativistic spin and crystal rotation symmetry, Phys. Rev. X **12**, 031042 (2022).

[13] I. I. Mazin, Notes on altermagnetism and superconductivity, arXiv:2203.05000.

[14] K. Koepernik and H. Eschrig, Full-potential nonorthogonal local-orbital minimum-basis band-structure scheme, Phys. Rev. B **59**, 1743 (1999).

[15] J. P. Perdew, K. Burke, and M. Ernzerhof, Generalized gradient approximation made simple, Phys. Rev. Lett. **77**, 3865 (1996).

[16] See Supplemental Material at http://link.aps.org/supplemental/10.1103/PhysRevB.109.L220412 for additional DFT results, more analysis of the altermagnetism, and details on the classical Monte Carlo calculations, which includes Refs. [8,19,32–37].

[17] D. M. Bishop, Molecular orbital energy levels for the sulfate ion, Theor. Chim. Acta **8**, 285 (1967).

[18] G. Höjer, S. Meza-Höjer, and G. Hernández de Pedrero, A CNDO study of the electronic structure of oxyanions XO_4^{n-} with $X =$ Si, P, S, Cl, Ge, As, Se and Br, Chem. Phys. Lett. **37**, 301 (1976).

[19] H. Kim, K. Shiozaki, and S. Murakami, Glide-symmetric magnetic topological crystalline insulators with inversion symmetry, Phys. Rev. B **100**, 165202 (2019).

[20] M. Naka, S. Hayami, H. Kusunose, Y. Yanagi, Y. Motome, and H. Seo, Spin current generation in organic antiferromagnets, Nat. Commun. **10**, 4305 (2019).

[21] K.-H. Ahn, A. Hariki, K.-W. Lee, and J. Kuneš, Antiferromagnetism in RuO$_2$ as d-wave Pomeranchuk instability, Phys. Rev. B **99**, 184432 (2019).

[22] S. Hayami, Y. Yanagi, and H. Kusunose, Momentum-dependent spin splitting by collinear antiferromagnetic ordering, J. Phys. Soc. Jpn. **88**, 123702 (2019).

[23] L. Šmejkal, R. González-Hernández, T. Jungwirth, and J. Sinova, Crystal time-reversal symmetry breaking and spontaneous Hall effect in collinear antiferromagnets, Sci. Adv. **6**, eaaz8809 (2020).

[24] S. Hayami, Y. Yanagi, and H. Kusunose, Bottom-up design of spin-split and reshaped electronic band structures in antiferromagnets without spin-orbit coupling: Procedure on the basis of augmented multipoles, Phys. Rev. B **102**, 144441 (2020).

[25] S. Chillal, Y. Iqbal, H. O. Jeschke, J. A. Rodriguez-Rivera, R. Bewley, P. Manuel, D. Khalyavin, P. Steffens, R. Thomale, A. T. M. N. Islam, J. Reuther, and B. Lake, Evidence for a three-dimensional quantum spin liquid in PbCuTe$_2$O$_6$, Nat. Commun. **11**, 2348 (2020).

[26] L. Heinze, H. O. Jeschke, I. I. Mazin, A. Metavitsiadis, M. Reehuis, R. Feyerherm, J.-U. Hoffmann, M. Bartkowiak, O. Prokhnenko, A. U. B. Wolter, X. Ding, V. S. Zapf, C. Corvalán Moya, F. Weickert, M. Jaime, K. C. Rule, D. Menzel, R. Valentí, W. Brenig, and S. Süllow, Magnetization process of atacamite: A case of weakly coupled $S = 1/2$ sawtooth chains, Phys. Rev. Lett. **126**, 207201 (2021).

[27] M. Hering, F. Ferrari, A. Razpopov, I. I. Mazin, R. Valentí, H. O. Jeschke, and J. Reuther, Phase diagram of a distorted kagome antiferromagnet and application to Y-kapellasite, npj Comput. Mater. **8**, 10 (2022).

[28] A. I. Liechtenstein, V. I. Anisimov, and J. Zaanen, Density-functional theory and strong interactions: Orbital ordering in Mott-Hubbard insulators, Phys. Rev. B **52**, R5467 (1995).

[29] G. Khaliullin, Orbital order and fluctuations in Mott insulators, Prog. Theor. Phys. Suppl. **160**, 155 (2005).

[30] J. Otsuki, K. Yoshimi, H. Shinaoka, and Y. Nomura, Strong-coupling formula for momentum-dependent susceptibilities in dynamical mean-field theory, Phys. Rev. B **99**, 165134 (2019).

[31] K. Momma and F. Izumi, *VESTA3* for three-dimensional visualization of crystal, volumetric and morphology data, J. Appl. Crystallog. **44**, 1272 (2011).

[32] H. O. Jeschke, F. Salvat-Pujol, E. Gati, N. H. Hoang, B. Wolf, M. Lang, J. A. Schlueter, and R. Valentí, Barlowite as a canted antiferromagnet: Theory and experiment, Phys. Rev. B **92**, 094417 (2015).

[33] K. Iida, H. K. Yoshida, A. Nakao, H. O. Jeschke, Y. Iqbal, K. Nakajima, S. Ohira-Kawamura, K. Munakata, Y. Inamura, N. Murai, M. Ishikado, R. Kumai, T. Okada, M. Oda, K. Kakurai, and M. Matsuda, $q = 0$ long-range magnetic order in centennialite CaCu$_3$(OD)$_6$Cl$_2 \cdot$ 0.6D$_2$O: A spin-$\frac{1}{2}$ perfect kagome antiferromagnet with J_1-J_2-J_d, Phys. Rev. B **101**, 220408(R) (2020).

[34] G. Kresse and J. Hafner, *Ab initio* molecular dynamics for liquid metals, Phys. Rev. B **47**, 558 (1993).

[35] G. Kresse and J. Furthmüller, Efficiency of *ab-initio* total energy calculations for metals and semiconductors using a plane-wave basis set, Comput. Mater. Sci. **6**, 15 (1996).

[36] G. Kresse and J. Furthmüller, Efficient iterative schemes for *ab initio* total-energy calculations using a plane-wave basis set, Phys. Rev. B **54**, 11169 (1996).

[37] G. Kresse and D. Joubert, From ultrasoft pseudopotentials to the projector augmented-wave method, Phys. Rev. B **59**, 1758 (1999).

CuAg(SO$_4$)$_2$: A doubly strongly correlated altermagnetic three-dimensional analog of the parent compounds of high-T_c cuprates
– Supplemental Material –

Harald O. Jeschke,[1] Makoto Shimizu,[2] and Igor I. Mazin[3]

[1] *Research Institute for Interdisciplinary Science, Okayama University, Okayama 700-8530, Japan*
[2] *Department of Physics, Graduate School of Science, Kyoto University, Kyoto 606-8502, Japan*
[3] *Department of Physics and Astronomy, and Quantum Science and Engineering Center,*
George Mason University, Fairfax, Virginia 22030, USA
(Dated: June 24, 2024)

Additional DFT results

In Fig. S1, we identify the character of the bands of CuAg(SO$_4$)$_2$ near the Fermi level by showing the Ag $4d$ and Cu $3d$ orbital weights, respectively. The local coordinate system is appropriately chosen with x and y pointing towards nearest Ag-O or Cu-O bonds and z pointing towards the apex of the elongated octahedra. The orbital character of the four bands at the Fermi level is dominated by Ag $4d_{x^2-y^2}$ and Cu $3d_{x^2-y^2}$. Note that

Figure S2. Integrated density of states of CuAg(SO$_4$)$_2$ at $U_\text{Ag} = 3.6\,\text{eV}$, $U_\text{Cu} = 4.8\,\text{eV}$ in the lowest energy antiferromagnetic state. This corresponds to the density of states shown in Fig. 3 of the main text. The electron count is shown per atom and per spin.

this figure shows nonmagnetic calculations without and DFT+U correction, before the magnetic order shifts different bands into each other. This way it shows more clearly that we have the $d_{x^2-y^2}$ bands near the Fermi level, and the weight is on different bands for Cu and for Ag.

Fig. S2 shows the integrated number of occupied and empty states for CuAg(SO$_4$)$_2$ in the lowest energy antiferromagnetic $\mathbf{q} = (0, 0, 2\pi)$ state. This is calculated with GGA+U at $U_\text{Ag} = 3.6\,\text{eV}$, $U_\text{Cu} = 4.8\,\text{eV}$ and corresponds to the density of state plot in Fig. 3 of the main text. Note that for total electron numbers, the values have to be multiplied by 2 for spin and by multiplicity in the formula, *i.e.* 2 for S and 8 for O.

In Fig. S3, we demonstrate the spin splitting in the lowest energy AFM state, *i.e.* the property of altermagnetism in CuAg(SO$_4$)$_2$. Fig. S3 (a) shows the bands along the $\Gamma - R$ path (see Figs. 2 (a) and (b) of the main text for the Ag $4d$ and Cu $3d$ orbital character, respectively). Fig. S3 (b) shows a small energy range, with
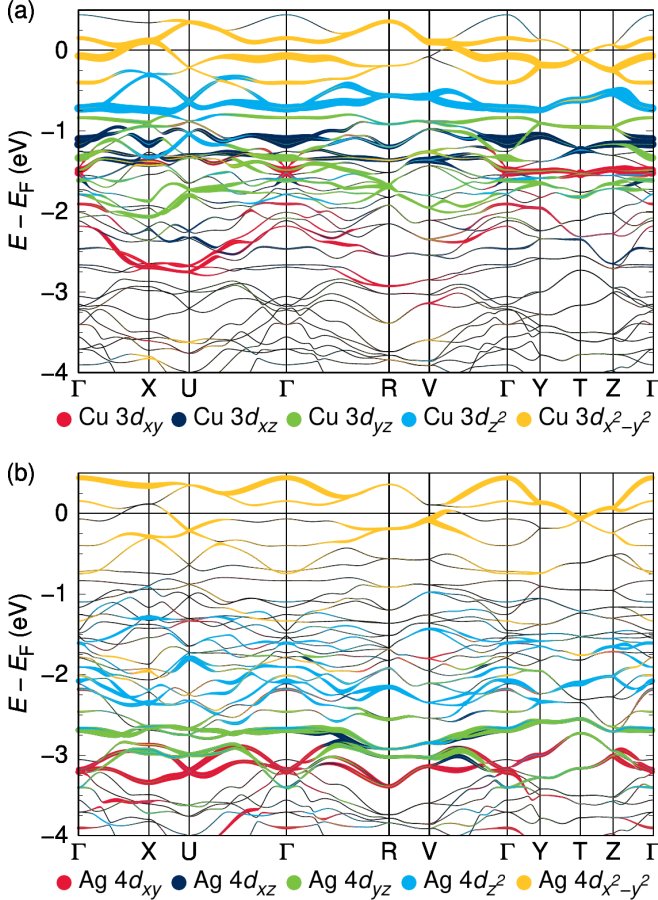

Figure S1. GGA band structure of CuAg(SO$_4$)$_2$ with (a) orbital weights of Cu and (b) of Ag. Cu $3d$ and Ag $4d$ orbital character, respectively, are highlighted.
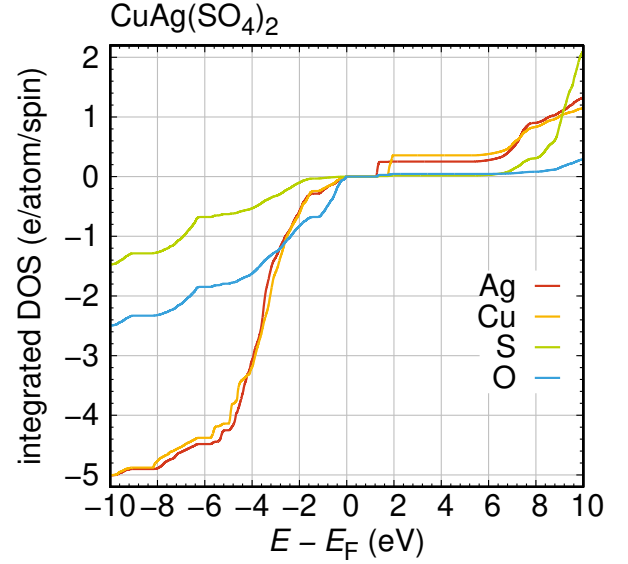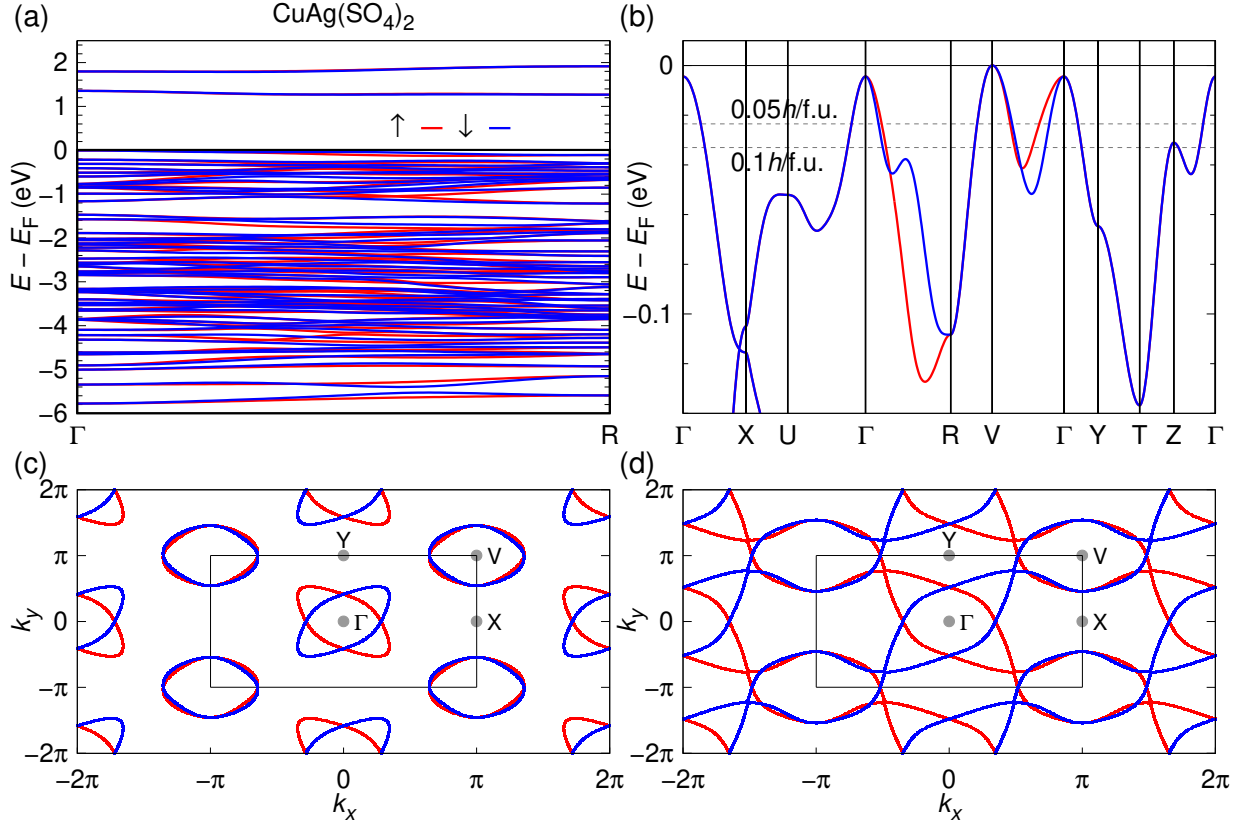
Figure S3. (a) Band structure of CuAg(SO$_4$)$_2$ in the lowest energy AFM state along the $\Gamma - R$ path, with spin up bands in red and spin down bands in blue. The spin splitting between up and down bands indicates altermagnetism. (b) Small energy range of the full band structure. Energies that correspond to doping with 0.05 and 0.1 holes per formula unit are marked by dashed lines. (c) and (d) Fermi surfaces of CuAg(SO$_4$)$_2$ in the $k_x - k_y$ plane under hypothetical doping by 0.05 and 0.1 holes per formula unit, respectively.

high symmetry points $X = (1/2, 0, 0)$, $U = (1/2, 0, 1/2)$, $R = (1/2, 1/2, 1/2)$, $V = (1/2, 1/2, 0)$, $Y = (0, 1/2, 0)$, $T = (0, 1/2, 1/2)$, $Z = (0, 0, 1/2)$. Dashed lines mark the energies $E = -23.5$ meV and $E = -33$ meV which would correspond to doping the formual unit with 0.05 and 0.1 holes, respectively. Figs. S3 (c) and (d) show Fermi surfaces under the assumption that doping with 0.05 and 0.1 holes per formula unit could be achieved. In the $k_x - k_y$ plane, these Fermi surfaces which are plotted here in the rigid band approximation would also be spin split due to the altermagnetic nature of CuAg(SO$_4$)$_2$.

Spin up and spin down sublattices in the $P2_1/n$ space group can be connected by a glide operation, $(x, y, z) \rightarrow (x + \frac{1}{2}, \bar{y} + \frac{1}{2}, z + \frac{1}{2})$. Therefore, the magnetic structure is preserved under a combination of the glide and time reversal operations, which maps

$$(k_x, k_y, k_z, \sigma) \rightarrow (k_x, -k_y, k_z, \sigma)$$
$$\rightarrow (-k_x, k_y, -k_z, \bar{\sigma}) \qquad \text{(S1)}$$

in momentum space [1]. In addition, the magnetic structure is preserved under the inversion operation. Therefore, the magnetic structure is also preserved under the

operation, which maps

$$(-k_x, k_y, -k_z, \bar{\sigma}). \rightarrow (k_x, -k_y, k_z, \bar{\sigma}) \qquad \text{(S2)}$$

in momentum space. Therefore, the electronic state at (k_x, k_y, k_z) of spin up is equivalent to those at $(-k_x, k_y, -k_z)$ and at $(k_x, -k_y, k_z)$ of spin down, and thus

$$E_\uparrow(k_x, k_y, k_z) = E_\downarrow(-k_x, k_y, -k_z)$$
$$E_\uparrow(k_x, k_y, k_z) = E_\downarrow(k_x, -k_y, k_z). \qquad \text{(S3)}$$

Band splitting in Fig. S3 (b) can be understood with Eq. (S3). The first equation leads to $E_\uparrow(\mathbf{k}) = E_\downarrow(\mathbf{k})$ on $(0, k_y, 0)$, $(0, k_y, \pi)$, $(\pi, k_y, 0)$ and (π, k_y, π) lines, which leads to no band splitting on the k-paths of Γ-Y and T-Z. The second equation leads to $E_\uparrow(\mathbf{k}) = E_\downarrow(\mathbf{k})$ on $k_y = 0, \pi$ planes, which leads no band splitting on the k-path of Γ-X-U-Γ, R-V, Y-T and Z-Γ. Therefore, bands can split on the k-paths of Γ-R and V-Γ.

The Fermi surface cuts in Fig. S3 (c,d) also reflect Eq. (S3). On the $k_z = 0$ plane, the equations become $E_\uparrow(k_x, k_y) = E_\downarrow(-k_x, k_y)$ and $E_\uparrow(k_x, k_y) = E_\downarrow(k_x, -k_y)$. Thus, the Fermi surface of up spin (red) coincides with that of down spin (blue) if it is rotated by 90 degrees around Γ.

Classical molecular field theory

Given the nontrivial exchange Hamiltonian, it is instructive to re-derive the classical molecular field (Weiss) theory specifically for this case. As usual, we introduce the Curie susceptibility $\chi(T) = \mu_{\mathrm{eff}}^2/3T$, where $\mu_{\mathrm{eff}}^2 = 3$ for $S = 1/2$. Let us assume that in an external field H the two sublattices, Ag and Cu, acquire magnetic moments M_A and M_C. From the previous section, in order of decreasing magnitude, the relevant exchange constants are $J_{AC} = J_4$, $J_{AA} = J_5^A$ and $J_{CC} = J_2^C$. The molecular field on the site A will be $2M_C J_4 + 4M_A J_5^A$, on C $2M_A J_4 + 2M_C J_2^C$. Thus the Weiss equation will be

$$M_A = (H + 2M_C J_4 + 4M_A J_5^A)\chi \qquad (S4)$$

$$M_C = (H + 2M_A J_4 + 2M_C J_2^C)\chi \qquad (S5)$$

Solving for M, the Curie-Weiss susceptibility

$$\chi_{\mathrm{CW}} = (M_A + M_C)/2H$$
$$= \chi \frac{\chi^{-1} - 2J_4 + J_5^A + J_2^C}{\chi^{-1} + 2J_5^A + J_2^C + 2\chi(2J_5^A J_2^C - J_4^2)} \qquad (S6)$$

Expanding $1/\chi_{\mathrm{CW}}$ in $1/T$, we get the Curie-Weiss law with the same $\mu_{\mathrm{eff}} = \sqrt{3}$ and $\theta_{\mathrm{CW}} = (2J_4 + 2J_5^A + J_2^C)S(S + 1)/3 = (2J_4 + 2J_5^A + J_2^C)/4$, the expression that we used above to fix U_{eff}. The reason why Ref. [2] found a surprisingly large $\mu_{\mathrm{eff}}^2 = 2.3^2 = 5.3$, corresponding to $S = 0.75$, rather than $S = 1/2$, is unclear at this point.

Comparison to cuprates

In Fig. S4, we show the density of states of the prototypical cuprate superconductor parent compound La_2CuO_4.

Additional DFT energy mapping details

In Table S1, we present the full results of the DFT energy mapping. They were obtained using a 5-fold unit cell of $CuAg(SO_4)_2$ containing ten formula units. This allows resolving all exchange interactions up to twice the nearest neighbor Ag-Cu distance of 3.58 Å. The Hund's rule coupling strength for Cu^{2+} is fixed at $J_H = 1\,\mathrm{eV}$ following previous work [3, 4]. We assume a factor 0.75 between $3d$ and $4d$ interaction values, thus fixing $J_H = 0.75\,\mathrm{eV}$ for Ag^{2+}. The error bars given in brackets reflect the statistical errors of the fit for the energies of 60 distinct spin configurations.

We demonstrate that the DFT energy mapping approach works extremely well in $CuAg(SO_4)_2$ by showing, in Fig. S5, a comparison between DFT energies and energies of the fitted Heisenberg Hamiltonian.
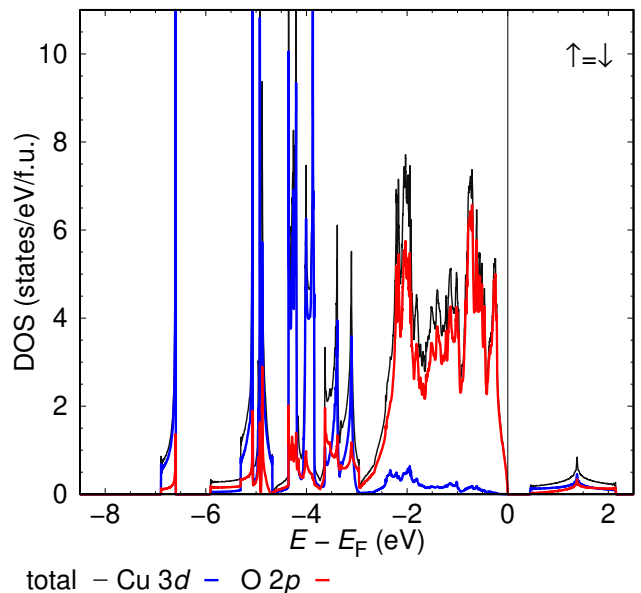

total — Cu 3d — O 2p —

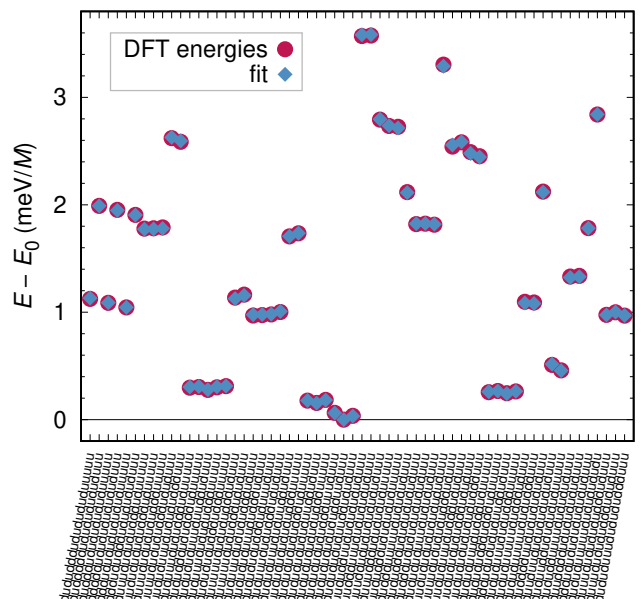Figure S4. GGA+U density of states of La_2CuO_4 in the Néel state. Spin ↑ and spin ↓ are identical so only spin ↑ is shown.

Figure S5. DFT energies for 60 spin configurations in a 5-fold unit cell of $CuAg(SO_4)_2$ at $U_{Ag} = 3.6\,\mathrm{eV}$, $U_{Cu} = 4.8\,\mathrm{eV}$, compared to the energies of the Heisenberg Hamiltonian with the fitted parameters given in the first line of Table S1. The fit is excellent.

Details of the classical Monte Carlo method

In the classical Monte Carlo (CMC) calculations, we perform the standard single spin-flip technique with Metropolis updates. We apply as many Metropolis updates as there are spins in the unit cell in each Monte Carlo step. For thermalization, we use 100,000 Monte

$M1\,M2$	U_{Ag}	U_{Cu}	J_1 AgCu	J_2^{A} AgAg	J_2^{C} CuCu	J_3 AgCu	J_4 AgCu	J_5^{A} AgAg	J_5^{C} CuCu	θ_{CW}
$d_{M1\,M2}$ (Å)			3.579	4.734		4.961	5.727	6.017		
	3.6	4.8	-3.6(1.2)	3.2(1.6)	35.2(9)	5.6(4)	169.5(4)	93.4(6)	-0.6(5)	-142
	3.65	**4.87**	**-3.4(1.2)**	**3.0(1.6)**	**34.4(9)**	**5.4(4)**	**168.6(4)**	**91.9(6)**	**-0.5(5)**	**-140**
	4.2	5.6	-1.5(9)	1.6(1.2)	26.7(6)	4.2(3)	150.3(3)	79.0(5)	-0.4(3)	-123
	4.8	6.4	-0.2(6)	0.6(9)	20.1(5)	3.4(2)	134.2(2)	68.5(4)	-0.3(3)	-108
	5.4	7.2	0.4(5)	0.1(7)	14.9(4)	2.8(2)	120.2(2)	61.0(3)	-0.2(2)	-96

$M1\,M2$	U_{Ag}	U_{Cu}	J_6 AgCu	J_7^{A} AgAg	J_7^{C} CuCu	J_8^{A} AgAg	J_8^{C} CuCu	J_{10} AgCu	J_{13} AgCu	J_{16}^{A} AgAg	J_{16}^{C} CuCu	θ_{CW}
$d_{M1\,M2}$ (Å)			6.134	6.215		7.158		8.332	8.846	9.266		
	3.6	4.8	-2.6(7)	-0.4(7)	-3.9(5)	-2.2(3.6)	0.5(1.2)	0.5(4)	0.4(2)	1.0(4)	0.0(3)	-142
	3.65	**4.87**	**-2.5(7)**	**-0.4(7)**	**-3.8(5)**	**-2.1(3.6)**	**0.5(1.2)**	**0.5(4)**	**0.3(2)**	**0.9(4)**	**0.0(3)**	**-140**
	4.2	5.6	-2.0(5)	-0.4(5)	-2.7(3)	-1.6(2.6)	0.3(9)	0.4(3)	0.2(2)	0.7(3)	0.0(2)	-123
	4.8	6.4	-1.6(4)	-0.4(4)	-2.0(3)	-1.2(1.9)	0.2(6)	0.3(2)	0.2(1)	0.5(2)	0.0(2)	-108
	5.4	7.2	-1.2(3)	-0.3(3)	-1.5(2)	-0.9(1.4)	0.2(5)	0.2(2)	0.1(1)	0.4(2)	0.0(1)	-96

Table S1. All calculated exchange parameters for $\mathrm{CuAg(SO_4)_2}$. The line in bold face is interpolated by demanding that the set of couplings yield the experimentally observed Curie-Weiss temperature of $\theta_{\mathrm{CW}} = -140\,\mathrm{K}$ [2].

Carlo steps. After thermalization, we use 10,000 Monte Carlo steps to measure physical quantities A. A averages are calculated from spin configurations at intervals of 10 Monte Carlo steps. In this study, A are total energy E, magnetization M and spin structure factor

$$S(\mathbf{q}) = \sum_{ij} \mathbf{S}_i \cdot \mathbf{S}_j e^{i\mathbf{q}\cdot(\mathbf{r}_i - \mathbf{r}_j)} \qquad (S7)$$

where $\mathbf{r}_i$ is the position of spin i. At the end of measurements, we calculate averages $\langle A \rangle_{\mathrm{MC}}$ of the measured physical quantities and calculate specific heat

$$C = k_{\mathrm{B}} \frac{\langle E^2 \rangle_{\mathrm{MC}} - \langle E \rangle_{\mathrm{MC}}^2}{T^2} \qquad (S8)$$

and susceptibility

$$\chi = \frac{1}{N} \frac{\langle \mathbf{M}^2 \rangle_{\mathrm{MC}} - \langle |\mathbf{M}| \rangle_{\mathrm{MC}}^2}{k_{\mathrm{B}} T} \qquad (S9)$$

where k_{B} is the Boltzmann constant, T is temperature, N is the number of spins in the unit cell, $\mathbf{M}$ is magnetization, and E is total energy. We repeat this set of thermalization and measurements 160 times and calculate average and standard deviations of C, χ and $\langle S(\mathbf{q}) \rangle_{\mathrm{MC}}$ for all sets.

Magnetooptics

In order to estimate the size of the altermagnetic effect in this compound we have calculated, using the built-in capability in the VASP code[5–8] (using *Ag_pv, Cu_pv, S and O* projector augmented wave potentials, energy cut-off of 400 eV, 500 valence bands, and a k-mesh of $9\times6\times9$) the full matrix dielectric function, assuming the Neél vector as suggested by the calculations, perpendicular to the ab plane, and found a sizeable antisymmetric contribution in the xz channel (note that symmetry also allows
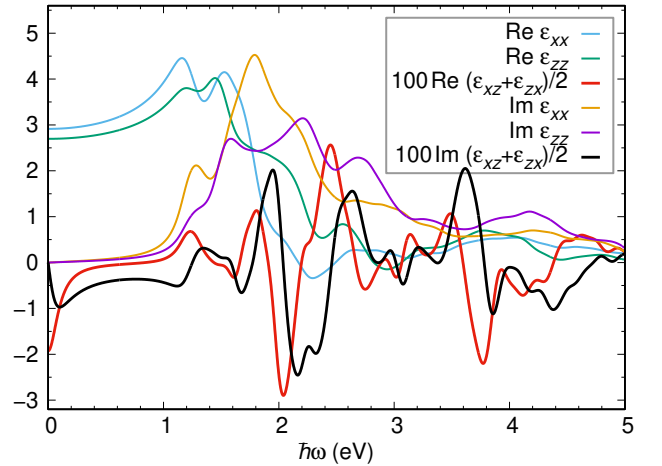

Figure S6. Calculated diagonal and asymmetric off-diagonal dielectric function. The latter is on the order of 1% of the former, which is considered sizeable in magnetooptics.

a nondiagonal *symmetric* ϵ_{xz}). The results are shown in Fig. S6.

Relativistic effects

We use fully relativistic GGA and GGA+U calculation in order to check for effects of spin-orbit coupling. Analyzing the total energies of the ground state AFM order in the unit cell of $\mathrm{CuAg(SO_4)_2}$, we find some anisotropy. At the GGA level, choosing x, y and z as magnetic quantization axis, we find moments to be easy axis along z with y direction 0.09 meV/f.u. higher and x 0.15 meV/f.u. higher in energy. At the relevant U value for $\mathrm{CuAg(SO_4)_2}$, $U_{\mathrm{Ag}} = 3.6$ eV, $U_{\mathrm{Cu}} = 4.8$ eV, x becomes easy axis with y direction 0.24 meV/f.u. higher

and z 1.4 meV/f.u. higher in energy.

[1] H. Kim, K. Shiozaki, and S. Murakami, Glide-symmetric magnetic topological crystalline insulators with inversion symmetry, Phys. Rev. B **100**, 165202 (2019).

[2] M. Domański, Z. Mazej, and W. Grochala, A unique two-dimensional silver(II) antiferromagnet $Cu[Ag(SO_4)_2]$ and perspectives for its further modifications, Chem. Eur. J. **29**, e202302042 (2023).

[3] H. O. Jeschke, F. Salvat-Pujol, E. Gati, N. H. Hoang, B. Wolf, M. Lang, J. A. Schlueter, and R. Valentí, Barlowite as a canted antiferromagnet: Theory and experiment, Phys. Rev. B **92**, 094417 (2015).

[4] K. Iida, H. K. Yoshida, A. Nakao, H. O. Jeschke, Y. Iqbal, K. Nakajima, S. Ohira-Kawamura, K. Munakata, Y. Inamura, N. Murai, M. Ishikado, R. Kumai, T. Okada, M. Oda, K. Kakurai, and M. Matsuda, $q = 0$ long-range magnetic order in centennialite $CaCu_3(OD)_6Cl_2 \cdot_0 \cdot 6 D_2O$: A spin-$\frac{1}{2}$ perfect kagome antiferromagnet with J_1-J_2-J_d, Phys. Rev. B **101**, 220408 (2020).

[5] G. Kresse and J. Hafner, Ab initio molecular dynamics for liquid metals, Phys. Rev. B **47**, 558 (1993).

[6] G. Kresse and J. Furthmüller, Efficiency of ab-initio total energy calculations for metals and semiconductors using a plane-wave basis set, Comput. Mater. Sci. **6**, 15 (1996).

[7] G. Kresse and J. Furthmüller, Efficient iterative schemes for ab initio total-energy calculations using a plane-wave basis set, Phys. Rev. B **54**, 11169 (1996).

[8] G. Kresse and D. Joubert, From ultrasoft pseudopotentials to the projector augmented-wave method, Phys. Rev. B **59**, 1758 (1999).